RESEARCH REPORT

VTT-R-00119-22

AM NPP - High temperature solution annealing of AM 316L

Authors: Tuomas Riipinen, Alejandro Revuelta, Antti Forsström, Zaiqing Que

Confidentiality: Public

Report's title AM NPP - High temperature solution annealing of AM 316L	
Customer, contact person, address SAFIR2022 Research Programme	**Order reference** Project AM-NPP
Project name Additive Manufacturing in nuclear power plants	**Project number/Short name** 128476 / AM-NPP 2021
Author(s) Tuomas Riipinen, Alejandro Revuelta, Antti Forsström, Zaiqing Que	**Pages** 27 p.
Keywords Additive manufacturing, 316L, Laser powder bed fusion, L-PBF, heat treatment, solution anneal, high temperature, material properties	**Report identification code** VTT-R-00119-22

Summary

The effect of different solution annealing (SA) treatments on the material properties of L-PBF produced 316L specimens was investigated. Hot Isostatic Pressing (HIP) is often the heat treatment of choice for L-PBF 316L as it results in good mechanical properties and isotropic microstructure, whereas the standard solution annealing cycle at 1066°C is not sufficient at homogenizing the material structure and properties. High temperature annealing was considered as an alternative for the more expensive HIP process, and according to published research, the higher annealing temperatures produce properties more close to conventionally manufactured alloy.

Cylindrical and rectangular bars were printed using L-PBF and the three different thermal post processes were applied: 1066°C/1h, 11150°C/1h and 1200°C/1h. All parts were heat treated in a vacuum furnace and stress relieved (650°C/2h) prior to solution annealing. The 1066°C annealing complies with the current 316L AM standard. After machining, characterization of mechanical properties was done by static tensile tests and Charpy-V impact tests. Samples were prepared for microstructure (SEM/EBSD) and chemical analysis.

The printed test specimen had very low porosity and a chemical composition comparable to the feedstock powder with no excess oxidation. The microstructure evolved from partially recrystallized and anisotropic at 1066°C to nearly fully recrystallized at 1200°C. The tensile properties decreased with increasing annealing temperature and fulfilled the minimum requirements specified in AM standard (R_e ≥ 205 MPa, R_m ≥ 515 MPa, A ≥ 30 %) in all conditions. The impact energies followed the same trend and for the 1200°C condition the average impact energy was below 40 J, which is the minimum requirement in standards SFS-EN 13480, SFS-EN 13445 that are relevant for materials used in nuclear applications.

Confidentiality	Public

Espoo 28.1.2022

Written by	**Reviewed by**	**Accepted by**
Tuomas Riipinen Research Scientist	Alejandro Revuelta Senior Scientist	Pasi Puukko Research Team Leader

VTT's contact address
VTT Ltd, POB 1000, FI-02044 VTT

Distribution (customer and VTT)

SAFIR2022 consortium, pdf
AM-NPP project consortium and STUK, pdf
VTT, original and pdf

Contents

1. Introduction and Objective

Initial results obtained during AM-NPP 2020 project together with DIVALIITO project (Metsä-Kortelainen *et al.*, 2020) supports the idea that the currently used solution annealing treatment profiles do not erase the anisotropic microstructure observed in the as-built material and that new heat treatment process conditions need to be used for Additively Manufactured (AM) components designed for nuclear applications. Nuclear grade materials need to meet specific requirements i.e. chemical and mechanical properties. Resistance to intergranular stress-corrosion cracking (IGSCC) is essential which is why nuclear grade stainless steels, most commonly the 304L and 316L, are the materials of choice for nuclear applications where good mechanical properties and excellent corrosion resistance are required (e.g. pressure vessels, piping). Material requirements for nuclear applications are specified in nuclear codes (e.g. RCC-M), guidelines (YVL guidelines) and standards (e.g. SFS-EN 13480, SFS-EN 13445). In addition to chemical and mechanical properties also other properties must be considered such as the maximum average grain size and the presence of delta ferrite phase among other properties (Division, 1985). A homogenous equiaxed grain structure is desirable as it provides good chemical resistance and isotropic properties at high operating temperatures.

The microstructure of L-PBF processed 316L is characterized by high anisotropy, dislocation density and residual stresses. While the AM processing results in higher material strength than conventional manufacturing due to different strengthening mechanisms, the as-processed material is most often unsuitable for demanding applications due to anisotropic mechanical properties (Charmi *et al.*, 2021) and worse SCC properties compared to annealed (Rebak and Lou, 2018). The material is therefore thermally processed to alter the microstructure and material properties. The heat treatments in current 316L AM standard (ASTM International, 2016) are adopted from practices in aerospace industry. While the HIP processing produces a microstructure similar to that conventional 316L the recommended solution annealing process does not produce homogenous microstructures and material properties.

While most studies related to AM of 316L investigate the material properties in the as-built state or after thermal processing at maximum of 1100°C, increasing number of research has been done on high temperature solution annealing. For conventionally manufactured 316L the heat treatment temperatures rarely exceed 1110°C and therefore temperatures above it are considered as high annealing temperatures. The research by (Voisin *et al.*, 2021) showed that high solution annealing temperatures led to homogenous grain structure, low densities or near absence of dislocations and mechanical properties similar to that of conventional well annealed 316L. They performed solution annealing cycles on L-PBF 316L parts at temperatures ranging from 400°C to 1200°C with a soaking time of 1h. Microstructure consisting almost entirely of near stress-free grains was obtained at temperatures of 1100°C and above while 1000°C was not sufficient at removing the highly anisotropic structure characteristic to L-PBF processed material. Also (Riabov *et al.*, 2021) reported similar mechanical properties for L-PBF processed material annealed at 1200°C for 1h. The strain rate was considerably higher after the high temperature anneal compared to intermediate annealing temperatures (400-800°C). The microstructure and mechanical properties of L-PBF 316L was also characterized by (Kong *et al.*, 2019) who also conducted corrosion tests on the material. Their observations regarding the microstructure and mechanical properties of material annealed at high temperature (1200°C) agree with other published research in that annealing at sufficiently high temperature produces homogenous crystal structure but also degrades the mechanical properties compared to as-built condition or lower annealing temperatures. The pitting corrosion potential decreased with increasing annealing temperature and for the AM sample (HT 1200°C) the pitting potential was similar to wrought 316L. (Lou *et al.*, 2017) reported on the crack growth behaviour of L-PBF manufactured 316L specimens in high temperature (288°C) water in different heat treatments conditions. The heat treatment HIP (1150°/4h, 1000 bar) + SA (1066°C/1h) produced a recrystallized grain structure with low porosity. Similar grain structure was observed and grain size as a sample (from a different vendor) which was solution annealed at 1150°C for 2h. The crack growth of the HIP + SA samples in high temperature

NWC (oxidizing normal water chemistry) and HWC (reducing hydrogen water chemistry) water were comparable to wrought and annealed 316L material. The SA sample had higher crack growth rate than the HIP + SA, which was likely a result of the higher porosity and pore size IN the SA sample.

The premise for using high temperature solution annealing is the possibility of having an alternative thermal processing method to the more traditional HIP process, which is considered as a suitable post processing route for AM 316L components for nuclear applications. The cost of post-processing could be reduced greatly if a similar microstructure and material properties were achievable by solution annealing compared to HIP'd alloy. The effect of high temperature solution annealing on the material properties of L-PBF produced 316L was investigated and the results are presented and discussed in this report.

2. Experimental Setup

2.1 Additive manufacturing

The AM equipment used for the experimental work is an SLM 125HL machine from SLM Solutions GmbH. This machine has a building platform of 125x125mm dimensions. The machine has as default oxygen, gas flow and humidity sensors. The build consisted of 10 square bars (57 mm × 7 mm × 7 mm) for machining impact specimens and 16 cylinder bars (11 mm × 110 mm) for tensile test specimens. The part layout and the heat treatment for each part are shown in Figure 1. The part in the middle of the build platform is a powder container which was not used in the project. Default 316L process parameters and scanning strategy for 30µm layer thickness provided by the machine manufacturer were used. The gas atomized feedstock powder was sourced from the OEM. The particle size distribution of the powder is $D_{V(25)}$=19µm, $D_{V(50)}$=30µm, $D_{V(90)}$=46µm as reported in previous research (Reijonen *et al.*, 2021). The powder was dried overnight in an argon protected furnace and sealed and fed to the machine before a print job.

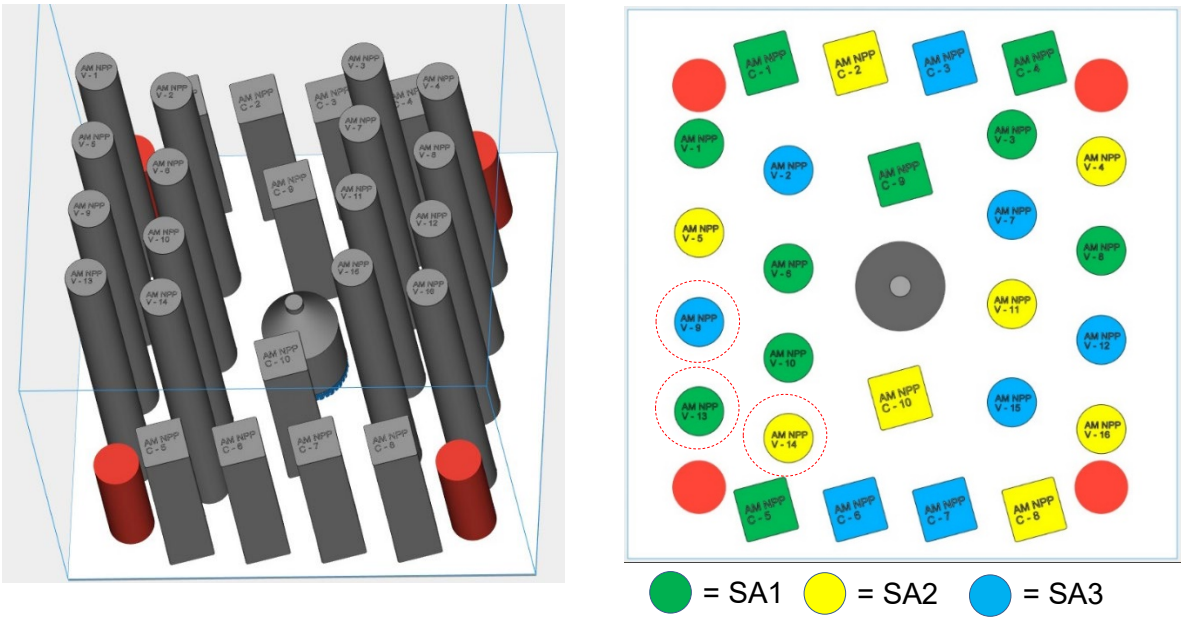

Figure 1. Left) Part layout , Right) Top view of the part layout with colours added to highlight the heat-treatment for each part. Parts marked with red circles were used for chemical, microstructure and porosity analysis.

2.2 Heat treatment

The post-thermal treatments for L-PBF manufactured 316L parts have been specified in the AM standard “F3184 − 16, Standard Specification for Additive Manufacturing Stainless Steel Alloy (UNS S31603) with Powder Bed Fusion”. According to the standard, the solution annealing cycle should conform to the AMS 2759 standard or Specification A484/A484M. In AMS 2759/4D “Heat Treatment, Austenitic Corrosion-Resistant Steel Parts” the solution annealing cycle has the following specifications: temperature = 1066°C, cooling method = air or equivalent, soaking time = 20 - 120 min depending on the thickness of maximum section. Regarding the furnace atmosphere, both air and protective atmospheres (argon, helium, hydrogen, neutral salt and vacuum) are accepted.

The parts were heat treated in a TORVAC Compact 30 model 1218 vacuum furnace. All parts were stress relieved prior to the solution annealing. For stress relieve the parts were kept at 650°C for 2 hours, using 4°C/min heating and cooling ramps. Three different solution annealing cycles were implemented (Table 1). The heat treatment “SA1” at 1066°C complies with the AMS 2759 standard and is used as the reference for the high temperature heat treatments.

Table 1. Solution annealing cycles

Heat treatment designation	Temperature [°C]	Soaking time [h]	Heating and cooling ramps [°C/min]
SA1	1066	1	4
SA2	1150		
SA3	1200		

2.3 Material Characterization

Tensile test specimens with 5 mm diameter and 25 mm gauge length were machined from the heat treated round bar samples. The specimen geometry and the test procedure conformed to ISO 6892-1:2016 standard. The tensile tests were conducted using Instron 1185 universal testing machine and altogether 15 specimens were tested, 5 per each heat treatment condition. The Charpy-V notch specimens were machined to the geometry specified in ISO 148-1:2016 and tested with Losenhausenwerk-MFL 1959. Three impact specimens were tested per each condition. All mechanical testing was conducted at room temperature.

The top sections (length ≈ 2.5 cm) of the printed and heat-treated cylinders were cut and used for microstructure and composition analysis as well as for measuring porosity. The pieces were cut in half with a blade saw, molded in resin, mechanically ground and polished down to 0.2 mm and then polished with a 0.05 mm non-crystallizing amorphous colloidal silica suspension. A field emission gun - scanning electron microscope (FEG-SEM) Zeiss Crossbeam 540 equipped with EDAXHikari Plus electron backscatter diffraction (EBSD) detector and solid-state four-quadrant backscatter detector (BSD) were used to characterize the polished cross sections and the fracture surface of the Charpy impact tested specimens. EBSD inversed pole figure (IPF) and kernel average misorientation (KAM) images acquired at ×200 magnification, 0.8 µm step size and with scale of 0–5° were analyzed by TSL OIM Analysis 8 software. The Inclusion chemical analysis by area mapping was performed with SEM- Energy Dispersive X-Ray (EDX). The same cross-sections were imaged with a ZEISS Axio Observer Inverted Microscope (×5 magnification). Porosity was measured from the images using ImageJ software (Fiji, GNU license) image analysis software. In all SEM, EBSD, and porosity analysis images, the AM build growth direction is vertical upward direction unless state otherwise.

The chemical composition was measured from the surface of the top sections of the tensile specimens using Optical Emission Spectrometer (OES) ARL iSpark 8860. Carrier gas method (Leco TC-500) was used to measure the Nitrogen and Oxygen contents of the printed specimens and the feedstock powder.

3. Results

3.1 Additive manufacturing

The printing process proceeded without issues and all of the parts (Figure 2) were built successfully. The oxygen content remained below the detection limit of the oxygen sensors in the built chamber during the build. No damage was observed in the recoater wiper or the parts.

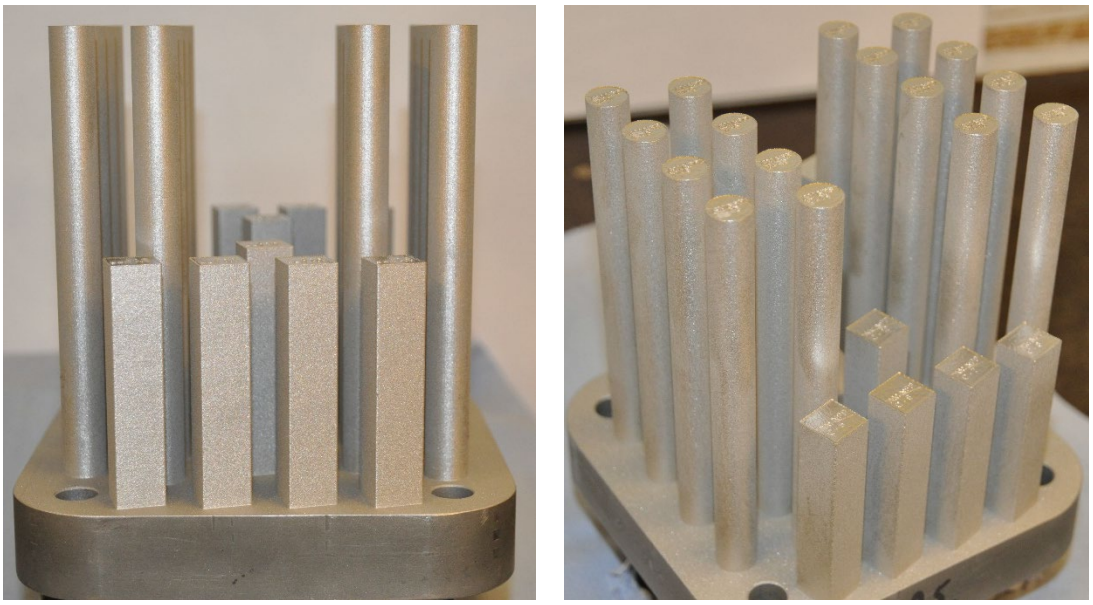

Figure 2. The printed test specimens

3.2 Chemical composition

The chemical compositions of feedstock powder and printed parts in different conditions are presented in Table 2. The chemical composition of DIVALIITO SA1 specimen and the values from the powder analysis certificate provided by the OEM are included in the table for comparison. The DIVALIITO specimen was manufactured from the same powder lot using the same process parameters as in AM NPP. There was no notable difference in chemical composition between DIVALIITO and AM NPP specimens. There was no difference in the measured Nitrogen and Oxygen contents of the powder compared to the values reported in the certificate.

Table 2. Chemical composition the feedstock powder and the heat-treated AM specimens

Element	SA1	SA2	SA3	DIVALIITO - SA1	316L powder (certificate)	316L powder (measured)
Fe	Bal.	Bal.	Bal.	Bal.	Bal.	
Cr	17.5	17.5	17.4	17.6	17.67	
Ni	12.5	12.5	12.4	12.5	12.61	
Cu	<0.01	<0.01	<0.01	0.02	-	
Mn	0.50	0.50	0.50	0.48	0.50	
Si	0.73	0.73	0.73	0.73	0.67	
Mo	2.29	2.31	2.29	2.43	2.33	
Al	0.003	0.003	0.002	0.003	-	
W	0.02	0.02	0.02	0.02	-	
V	0.025	0.024	0.026	0.027	-	
Ti	0.003	0.003	0.003	0.003	-	
Co	0.027	0.026	0.027	0.013	-	
C	0.014	0.013	0.012	0.010	0.016	
S	0.007	0.007	0.006	0.006	0.005	
P	0.008	0.008	0.008	0.010	0.008	
N	0.086	0.080	0.084	0.084	0.09	0.090
O	0.028	0.032	0.029	0.026	0.03	0.029

3.3 Mechanical properties

3.3.1 Tensile tests

The results of the tensile tests are shown in Table 3. Specimens solution annealed at 1066 °C have the highest yield ($R_{p0.2}$) and ultimate (R_m) tensile strengths, the averages being 329 ± 5.3 MPa and 573 ± 3.4 MPa, respectively. The average elongation to fracture, measured from an initial gauge length of 25 mm (A_{25mm}), of those specimens is 58.6 %. The average elongation to fracture of specimens solution annealed at 1200 °C is slightly higher at 61.3 %, but the average of yield and ultimate tensile strengths are considerably lower, being 248 ± 0.8 MPa and 566 ± 1.4 MPa, respectively. Specimens in all conditions fulfil the minimum tensile requirements specified in the ASTM F3184-16 standard.

Some of the specimens had distinct upper (R_{eh}) and lower (R_{el}) yield strengths. Specimen V-13 had the largest difference (R_{eh} - R_{el}) of 49.3 MPa. Figure 3 shows the engineering stress-strain curve obtained for specimen V-13. Displacements for strain calculation were measured

with a clip on extensometer. The total strain of the specimen gauge length is a bit higher as strain often localizes outside of the measurement area of the extensometer at the end of the test when necking occurs.

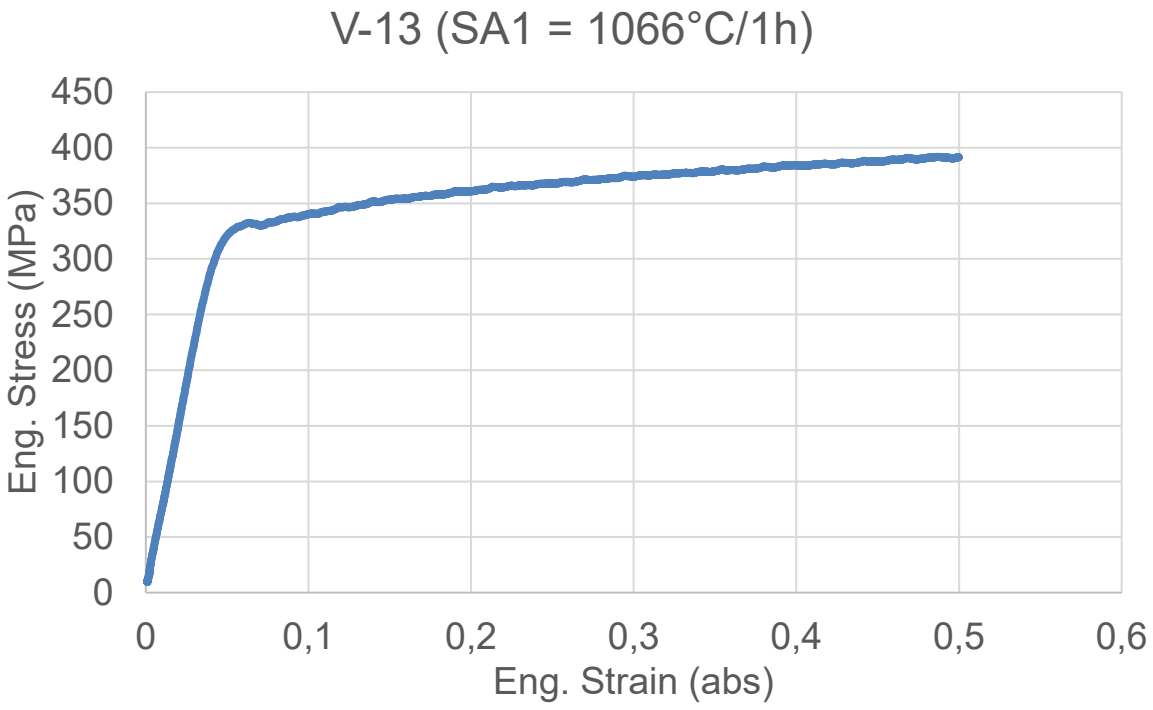

Figure 3. Engineering stress-strain curve of specimen V-13.

Heat treatment	Specimen	E (GPa)	R_{eh} (MPa)	R_{el} (MPa)	R_{eh}-R_{el}	$R_{p0.2}$ (MPa)	R_m (MPa)	A_{25mm} (%)
SA1 (1066°C)	V-3	187	414	368	46	329	574	58
	V-6	194	413	366	47	329	572	58
	V-8	193	371	368	3	323	575	57
	V-10	206	411	364	47	328	567	60
	V-13	194	421	372	49	338	574	60
	Average	**195**	**406**	**367**	**38**	**329**	**572**	**59**
	Std	**7**	**20**	**3**	**20**	**5**	**3**	**1**
SA2 (1150°C)	V-4	201	259	253	6	255	570	59
	V-5	182	262	252	11	255	570	59
	V-11	180	259	249	10	255	569	60
	V-14	195	262	247	15	253	568	62
	V-16	200	265	248	17	254	569	61
	Average	**192**	**262**	**250**	**12**	**254**	**569**	**60**
	Std	**10**	**3**	**2**	**4**	**1**	**1**	**1**
SA3 (1200 °C)	V-2	195	258	242	17	248	566	61
	V-7	201	260	242	17	248	565	63
	V-9	186	257	243	14	247	564	63
	V-2	194	259	242	17	249	568	60
	V-15	195	258	242	16	247	567	60
	Average	**194**	**258**	**242**	**16**	**248**	**566**	**61**
	Std	**5**	**1**	**0**	**1**	**1**	**1**	**2**

Table 3. Results of the static tensile tests

3.3.2 Impact tests

The impact toughness's obtained with the Charpy-V notch specimens in room temperature are shown in Table 4 together with the specimen dimensions. The highest impact toughness's were obtained with specimens C4 and C5 heat treated in 1066 °C. The lowest values were obtained with specimens C6 and C7 heat treated in 1200 °C. The deviation in impact energies were higher for SA1 and SA3 than SA2. Overall the average impact energies were low especially for specimens solution annealed at 1150°C and above. The dimensional tolerances for Charpy-V specimens as specified in SFS-EN ISO 148-1-2016 standard are; 54.4 ≤ length (L) ≤ 55.6, 9.925 ≤ width (W) ≤ 10.075, 9.89 ≤ thickness (B) ≤ 10.11. All specimens fulfilled the dimensional tolerance requirements as indicated in Table 2. The standard ASTM F3184-16 has no mention of minimum requirements for impact energies but in the standards SFS-EN 13480 "Metallic industrial piping" and SFS-EN 13455 "Unfired pressure vessels" the minimum impact energy obtained from Charpy-V impact tests (EN ISO 148-1:2010) at 20°C test temperature is defined as ≥ 40 J for austenitic stainless steels. Two impact specimens with SA3 treatment do not fulfil the impact energy requirement of 40 J.

Heat treatment	Specimen	Impact energy [J]
SA1 (1066°C)	C4	121
	C5	101
	C9	65
	Average	**96**
	Std	**28**
SA2 (1150°C)	C2	87
	C8	72
	C10	74
	Average	**78**
	Std	**8**
SA3 (1200°C)	C3	73
	C6	39
	C7	27
	Average	**46**
	Std	**24**

Table 4. Results of the impact tests

3.4 Porosity

The polished sample cross-section images used for optical image analysis are shown in Figure 4. As the results in Table 5 indicate the parts have very low porosity and only few larger pores were observed with diameter close to 100µm. The pores appeared to be randomly distrivuted in the analysed specimens.

Table 5. Measured porosities of printed 316L specimens

Sample ID	HT	Measurement area (mm2)	Porosity (%)
V-13	SA1	204	0.01
V-14	SA2	211	0.02
V-9	SA3	211	0.02

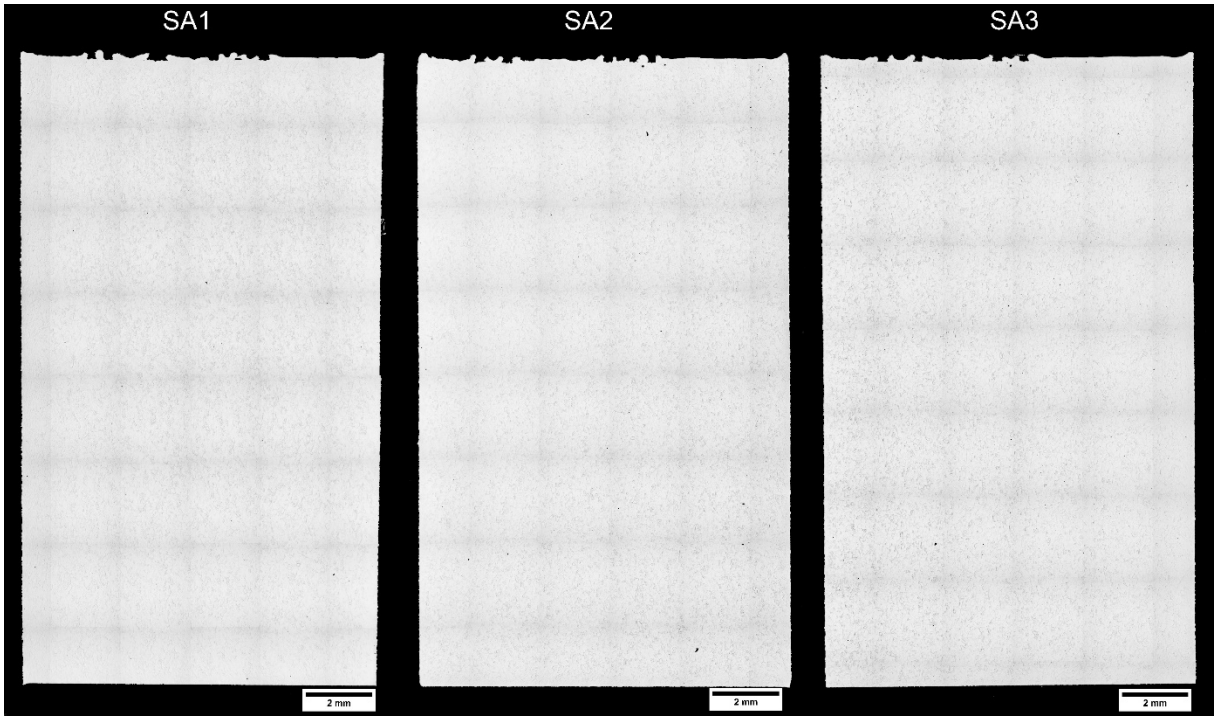

Figure 4. OM images of polished cross-sections used for porosity analysis

3.5 Microstructure

3.5.1 SEM/EBSD

The polished cross-sections (Figure 4) were analysed using SEM and the main findings are shown in Figures 5 and 6 for SA1, Figures 7-9 for SA2 and Figures 10-12 for SA3. A side-by-side comparison of the SEM images is shown in Figure 13. The SEM analysis revealed that the 1066°C solution anneal (SA1) resulted in a highly anisotropic crystal structure with high degree of low-angle grain boundaries characteristic to L-PBF processed material. The standard SA heat treatment was not sufficient at homogenizing the microstructure, which is a very common observation in published research. However, a small fraction of stress-free recrystallized grains was observed. For the SA2 (1150°C) specimen the grain structure consisted mostly of recrystallized grains but some un-recrystallized grains showing concentrations of low angle grain boundaries were found. For the SA3 (1200°C) specimen a nearly complete recrystallization structure was observed but few un-recrystallized grains still existed. The recrystallized grains have high angle grain boundaries while the non-recrystallized grains have low angle boundaries. The portion of the twin boundaries and high angle boundaries gradually increase with the increase of the SA temperature. The grain boundaries of all samples were decorated with non-metallic inclusions that increased in size with increasing annealing temperature and the inclusions were the largest in the SA3 specimen.

SA1

SEM images (SE2 and BSE) of SA1 specimen at three magnifications are shown in Figure 5. The SE2 images (left) better reveal the inclusions and the BSE images (right) makes it easy to distinguish individual grains. The grain structure is mostly anisotropic but few recrystallized were observed. The images with × 2000 magnification reveal the inclusions that decorate the grains as well as the grain boundaries. The microstructure was also analysed using an EBSD detector and the EBSD inversed pole figure (IPF) and kernel average misorientation (KAM) images are shown in Figure 6. The EBSD images clearly reveal the high degree of anisotropy in the specimen as well as few recrystallized grains. The KAM maps shows the residual strain/stress in the areas that have not recrystallized.

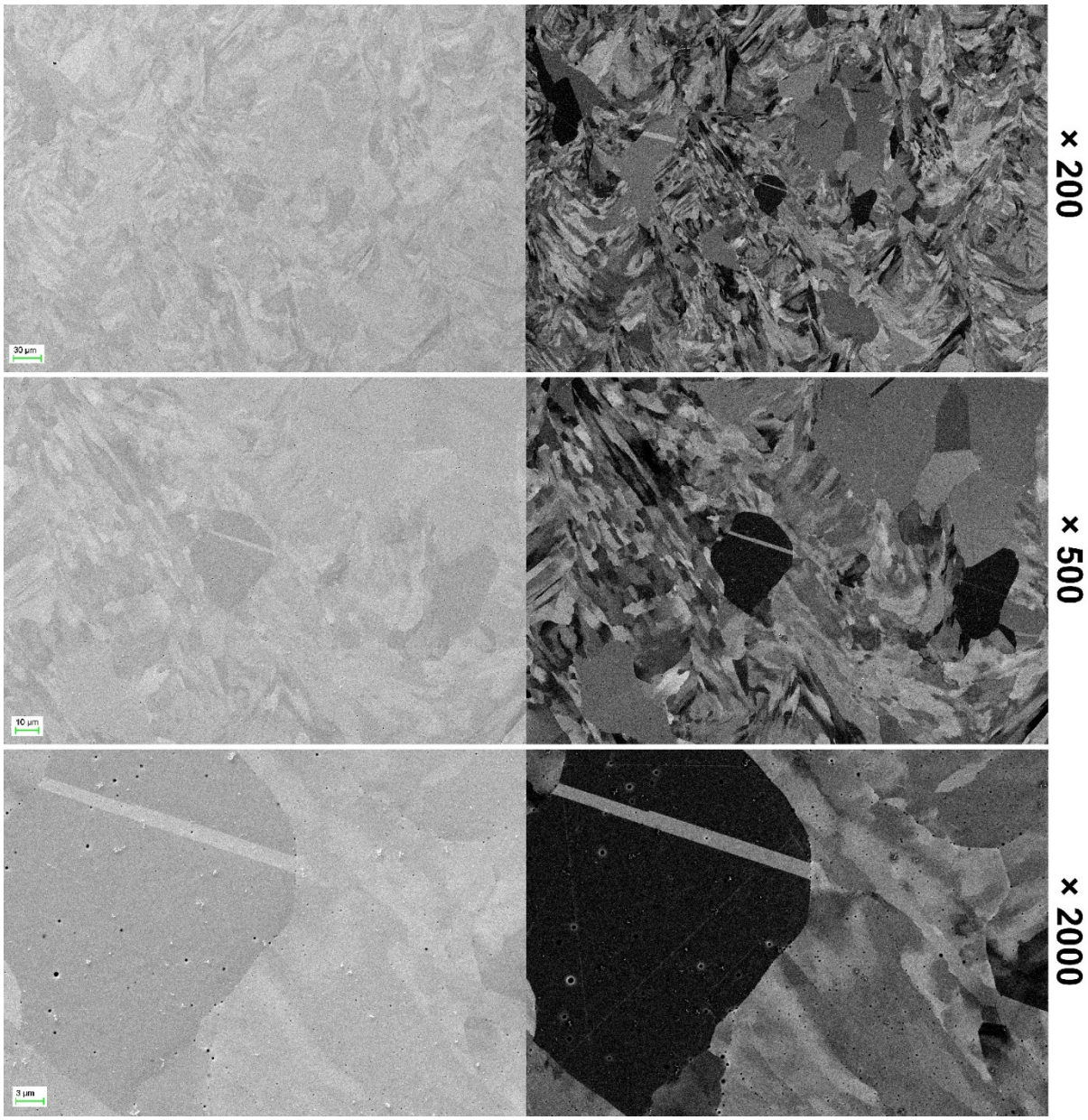

Figure 5. SE2 (left) and BSE (right) SEM images of SA1 sample with different magnifications

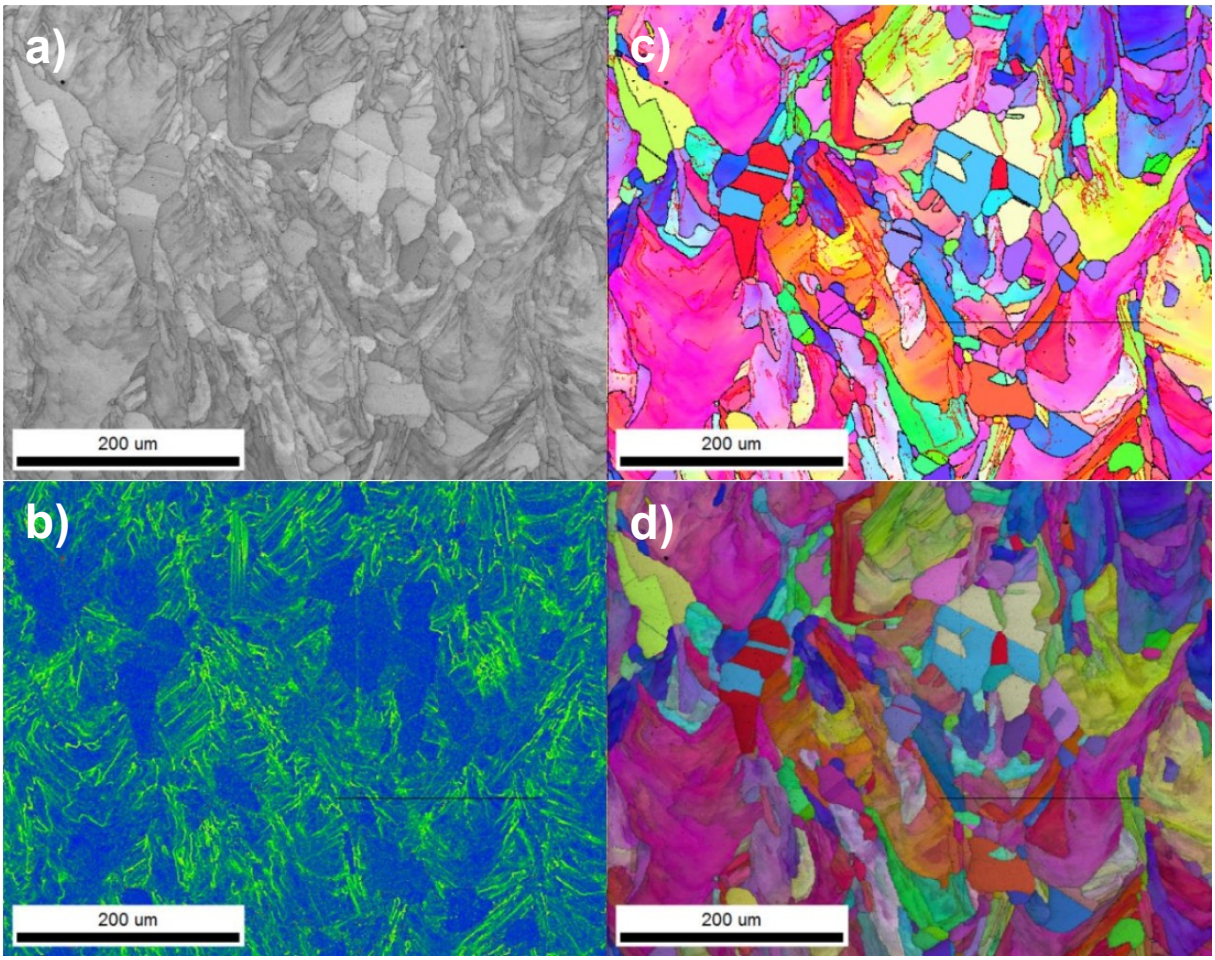

Figure 6. SEM images of SA1 specimen: a) SE2 image b) KAM map, c-d) EBSD IPF maps

SA2

SEM images (SE2 and BSE) of SA2 specimen at three magnifications are shown in Figure 7. The anisotropy found in the SA1 specimen has mostly disappeared after annealing at 1150°C, which resulted in a more homogenous crystal structure consisting mostly of equiaxed grains and annealing twins. Few un-recrystallized grains were observed and one is shown Figure 8. The isotropic structure can be seen more clearly in the EBSD IPF images (Figure 9). The KAM maps show some areas with high number of misorientations that were formed by rapid solidification during the L-PBF process. As with SA1, the SA2 specimen is decorated with non-metallic inclusions. The size of the inclusions appear slightly larger compared to SA1 specimen.

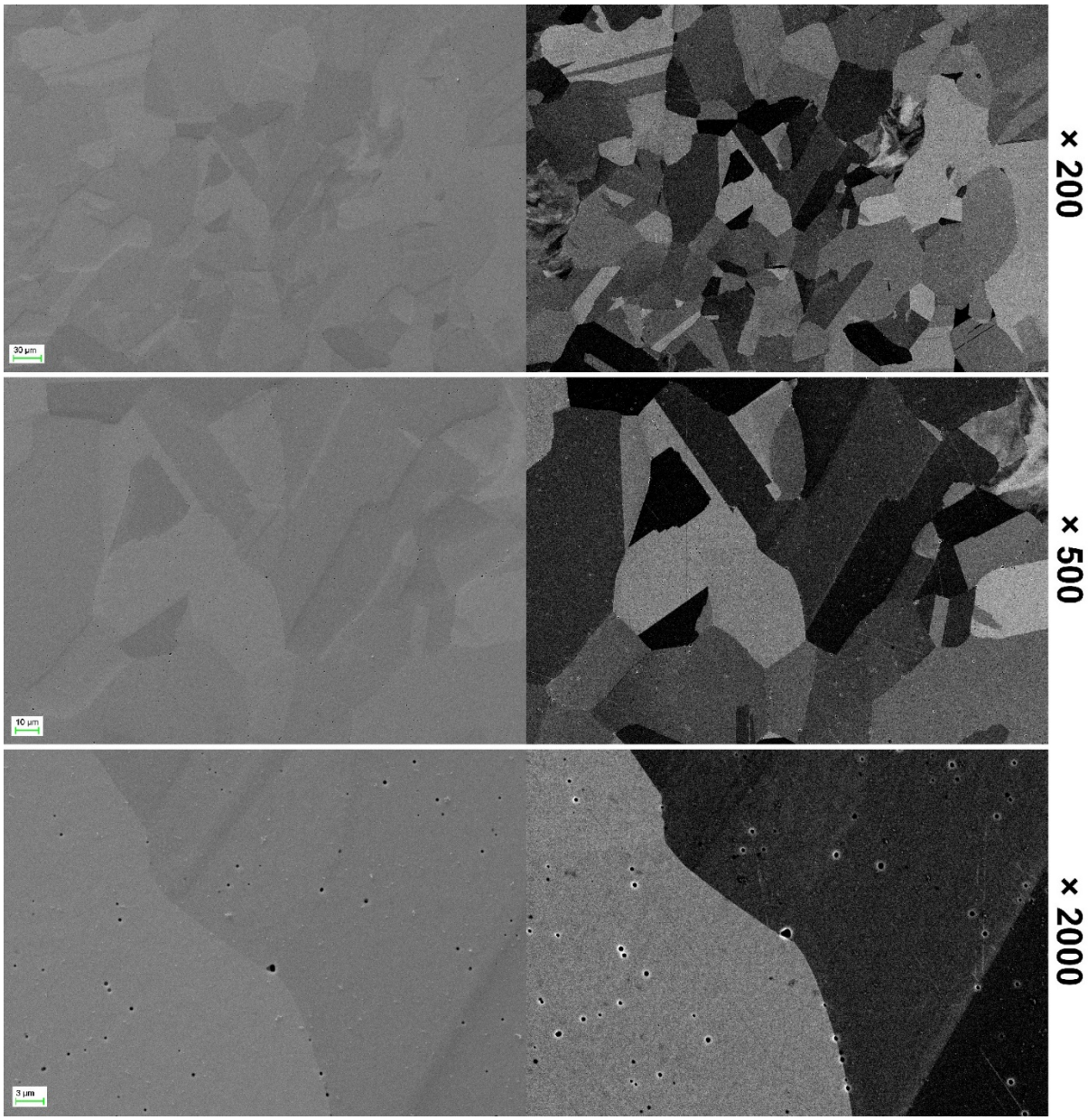

Figure 7. SE2 (left) and BSE (right) SEM images of SA2 sample with different magnifications

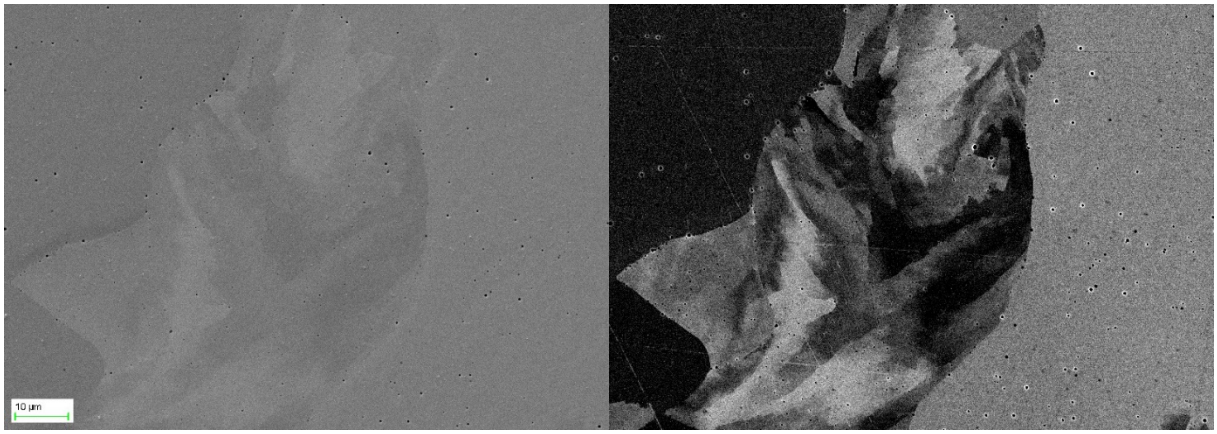

Figure 8. Areas of un-recrystallized grains, (left) SE2 image, (right) BSE image

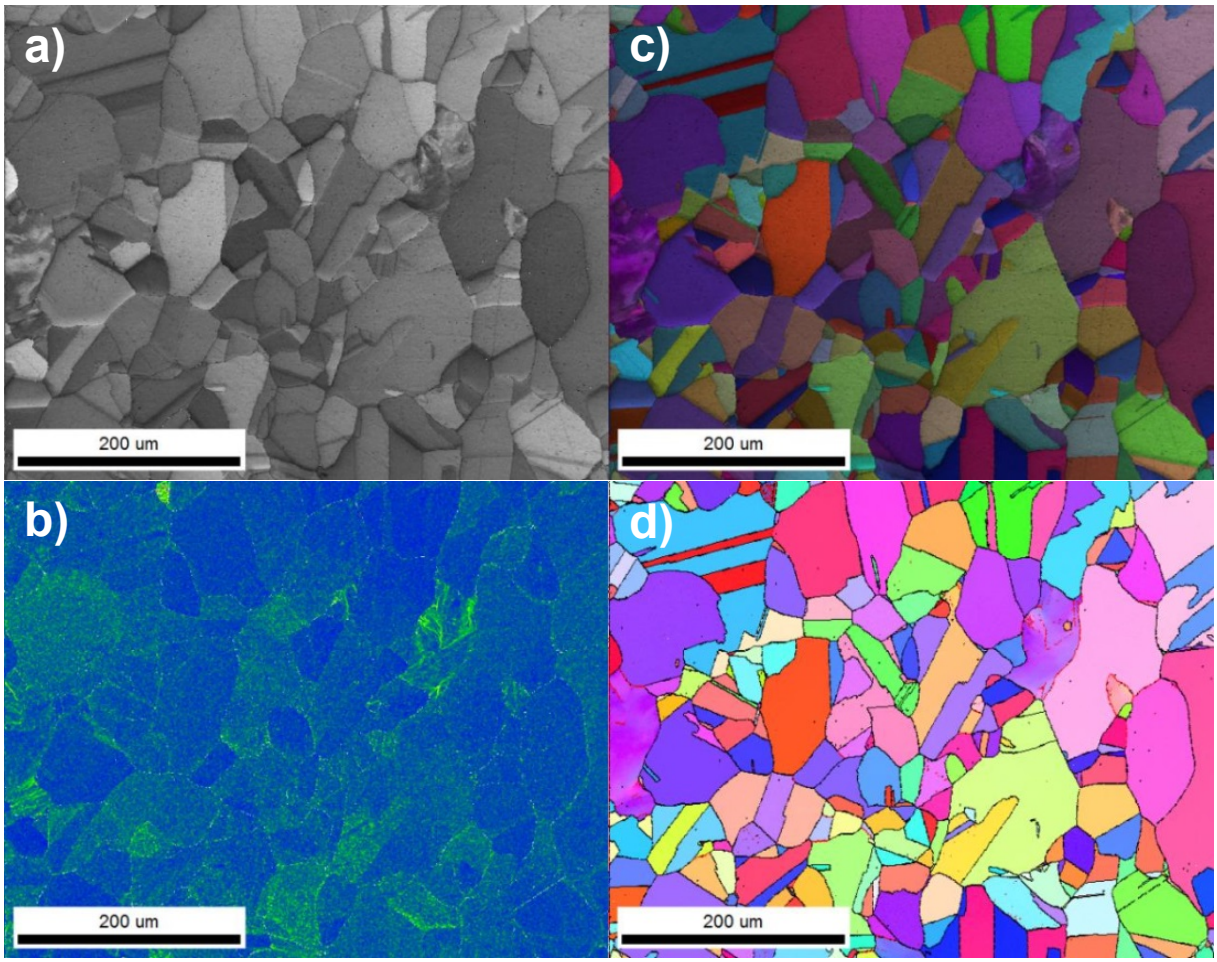

Figure 9. SEM images of SA2 specimen: a) SE2 image b) KAM map, c-d) EBSD IPF maps

SA3

SEM images (SE2 and BSE) of SA3 specimen at three magnifications are shown in Figure 10. The crystal structure has almost fully recrystallized after annealing at 1200°C. However, few un-recrystallized grains remain as shown in Figure 11. A clear difference between SA2 and SA3 is the size of the non-metallic inclusions which are larger after heat treating at a higher temperature (Figure 11). The KAM map (Figure 12) shows a decrease in the measured misorientations compared to SA2 with higher annealing temperature and the resulting crystal structure after annealing at 1200°C is primarily stress-free. The evolution of the microstructure is more clearly visible in Figure 13.

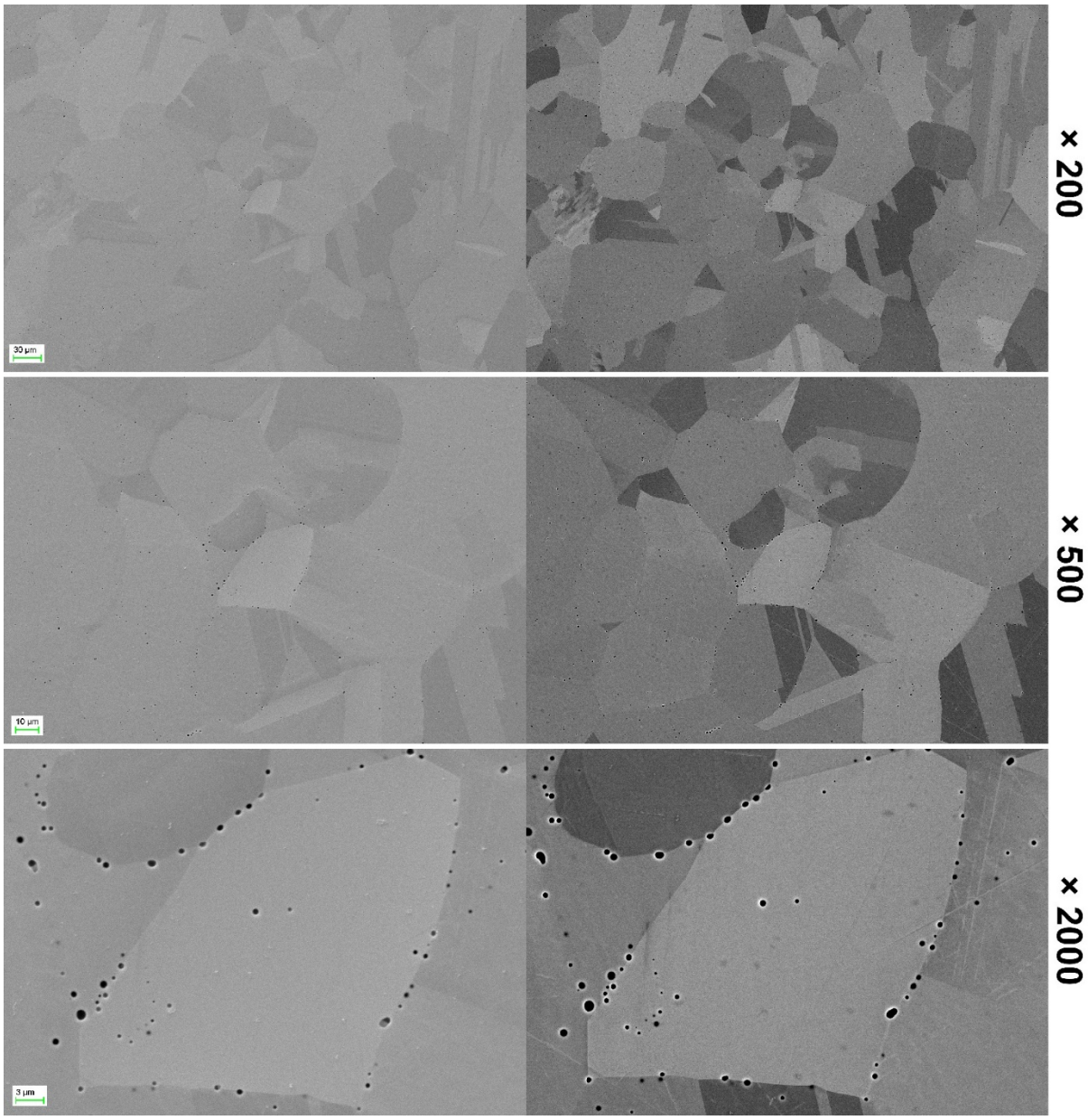

Figure 10. SE2 (left) and BSE (right) SEM images of SA3 sample with different magnifications

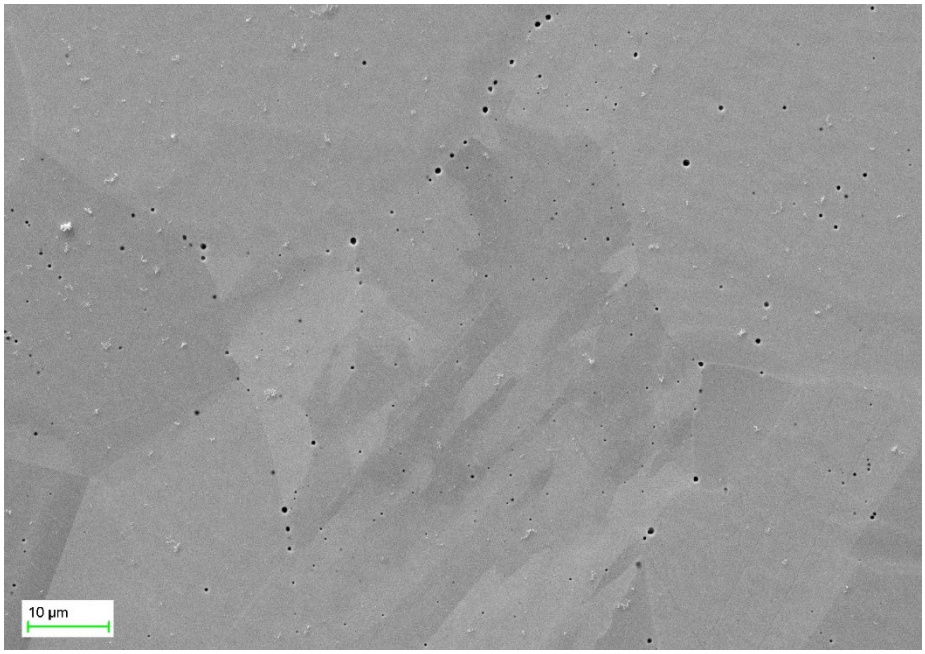

Figure 11. Areas of un-recrystallized grains, (left) SE2 image, (right) BSE image

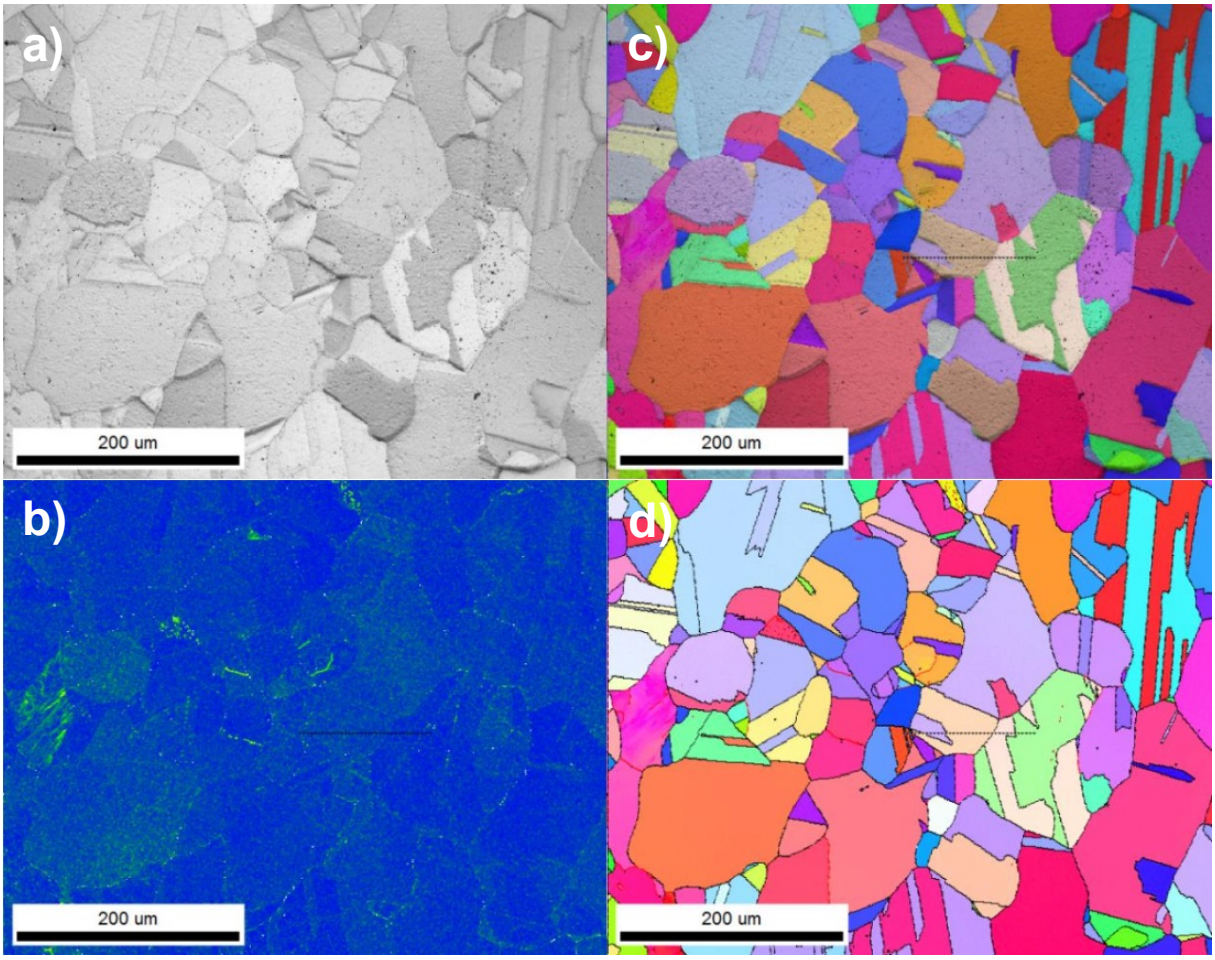

Figure 12. SEM images of SA3 specimen: a) SE2 image b) KAM map, c-d) EBSD IPF maps

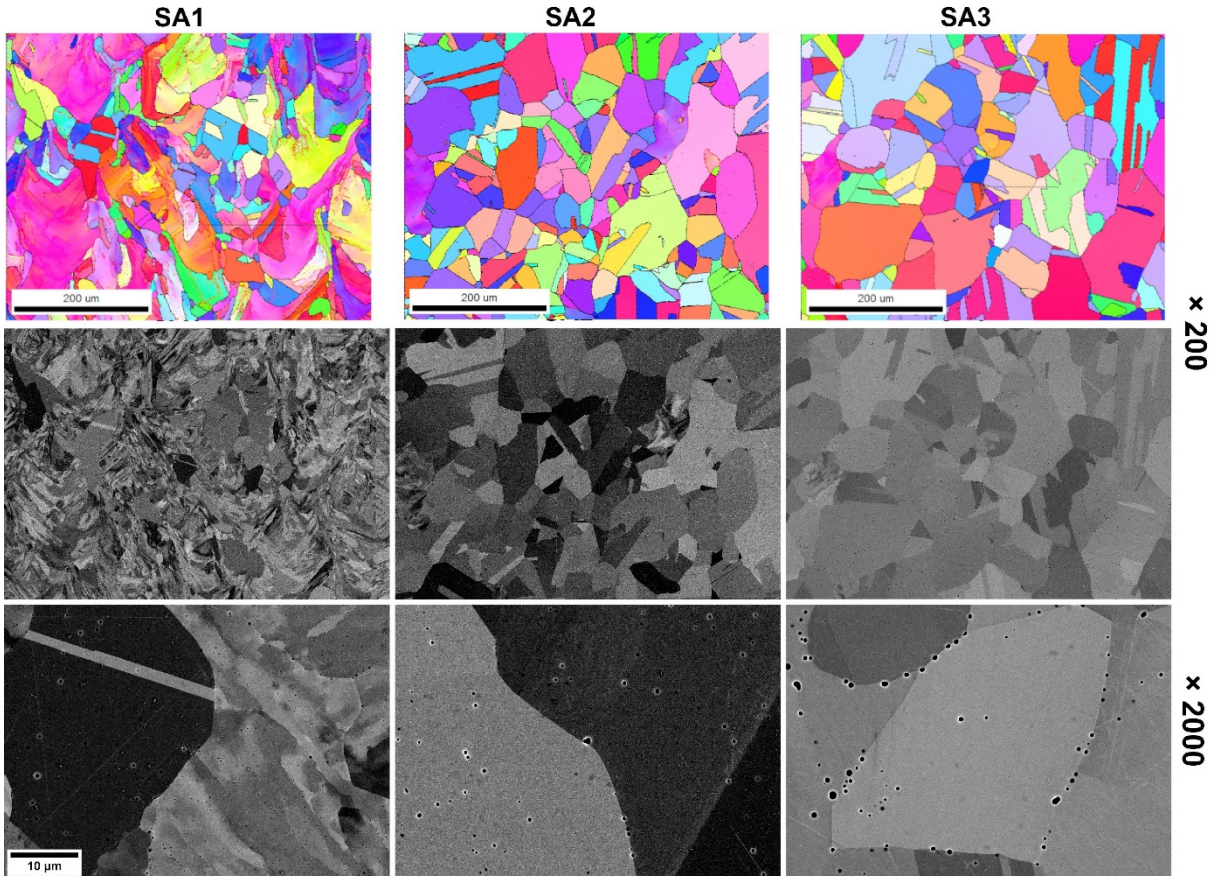

Figure 13. Side-by-side comparison of SA1, SA2 and SA3 SEM/EBSD images

3.5.2 Inclusion analysis (SEM/EDS)

Chemical analysis of the inclusion was performed with SEM- Energy Dispersive X-Ray (EDX) area mapping. Two areas of SA3 specimen were analysed (Figure 14) and the non-metallic inclusions were SiO_2 (black, round) and MnS inclusions (grey, oval). MnS inclusion is visible in the elemental analysis of Area 2 in Figure 14. Most of the inclusions were SiO_2 which were abundant in all of the analysed specimens.

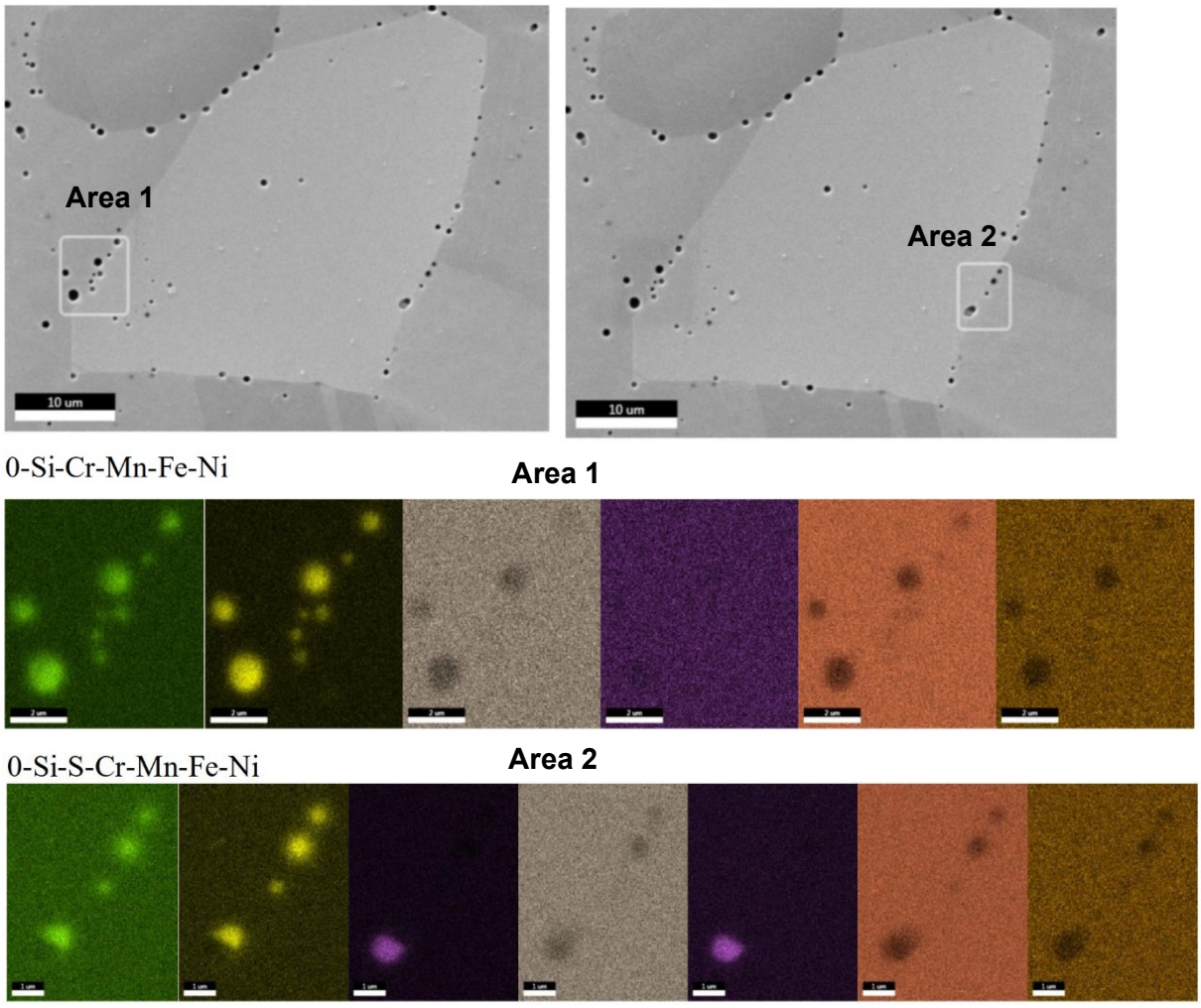

Figure 14. SEM- Energy Dispersive X-Ray (EDX) of non-metallic inclusions in SA3 specimen. Two areas were measured (Area1 & 2) and the composition maps below the SEM images include elements O, Si, Cr, Mn, Fe and Ni for Area 1 and O, Si, S, Cr, Mn, Fe, Ni for Area 2

3.5.3 Fracture surfaces

The fracture surfaces of SA1, SA2 and SA3 specimen are shown in Figures 15, 16 and 17 respectively. The magnifications are ×200 for the images on the left and ×5000 on the right. The primary fracture mode for all studied specimens was ductile dimple fracture, where the dimple size varies between regions of recrystallized and un-recrystallized grains. The rough fracture surface topology of SA1 and SA2 specimens indicate the presence of secondary cracking but the fracture surface of SA3 is smoother. The region in the middle of Figure 15 (right) shows an un-recrystallized area (grain) with significantly smaller dimple size compared to the regions on either sides that are recrystallized grains. Few inclusions are visible inside the dimples that act as void nucleation sites for fractures. The area of SA2 specimen shown in Figure 16 (right) is for an unrecrystallized grain.

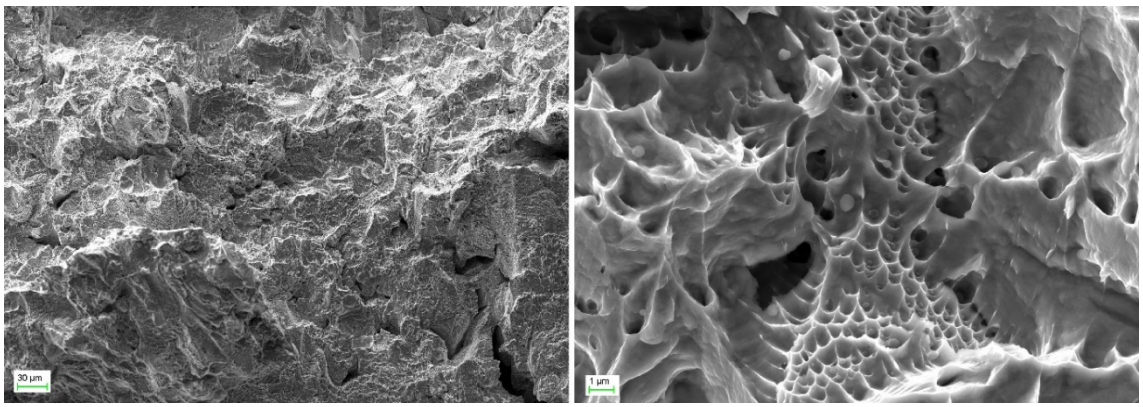

Figure 15. SEM images of SA1 Charpy-V specimen fracture surfaces with ×200 (left) and ×5000 (right)

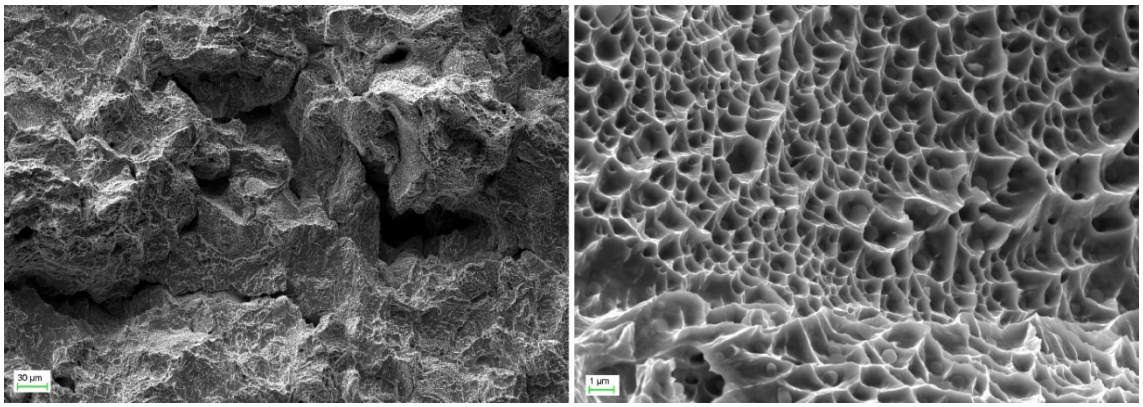

Figure 16. SEM images of SA2 Charpy-V specimen fracture surfaces with ×200 (left) and ×5000 (right)

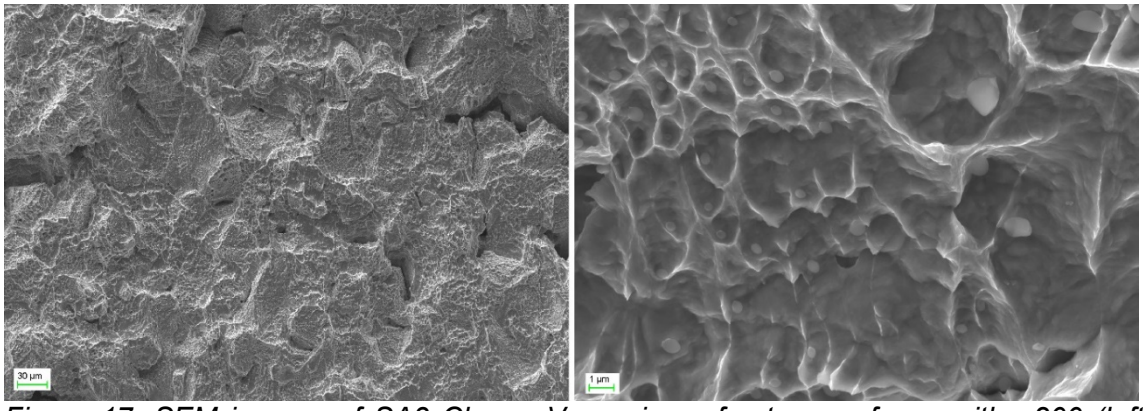

Figure 17. SEM images of SA3 Charpy-V specimen fracture surfaces with ×200 (left) and ×5000 (right)

4. Comparison of results (AM NPP and DIVALIITO projects)

Nearly identical experimental trial as described in this report was conducted in DIVALIITO project (Metsä-Kortelainen *et al.*, 2020). The results of the study have been published in a peer-reviewed journal (Reijonen *et al.*, 2021). Nearly identical experimental arrangement was implemented in AM NPP in order to have as comparable results as possible. The similarities between the experiments are: powder from the same powder lot was used, identical process parameters, pre-processing practices and L-PBF system were used, the part layout was identical and the heat treatment cycle SR + SA@1066°C was conducted for parts from both builds. The most significant difference between the two experiments in the thermal post processing as in the DIVALIITO project the printed parts were subject to stress-relieving (SR), SR + SA at 1066°C and SR + HIP (1150°C/4h, 1000 bar) processing. Comparing the results of the two projects provides insight on the variability of material properties of the same powder lot used at different points of time with the same process conditions.

4.1 Mechanical properties

Tensile and impact test specimens with the same geometry and dimensional tolerances were used for both projects. The tensile testing equipment and parameters were the same in the DIVALIITO project but a different machine was used for impact tests (Otto Wolpert Werke Gmbh Typ PW 30/15-E). All test were carried out in room temperature. The results of the static tensile tests and impact tests from both projects are shown in Figure 18 and Figure 19 respectively. In addition, stress relieved condition was studied in the DIVALIITO project, but is not included in the comparison from here on, as the focus is on solution annealing and HIP treatments.

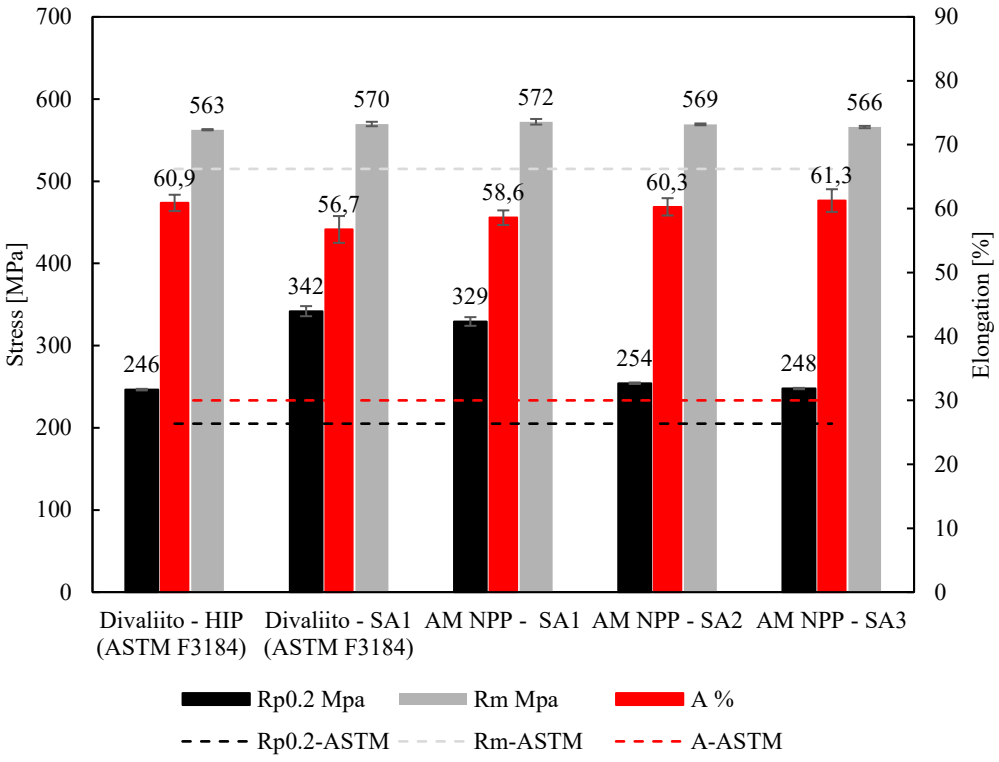

Figure 18. Tensile properties from AM NPP and DIVALIITO projects

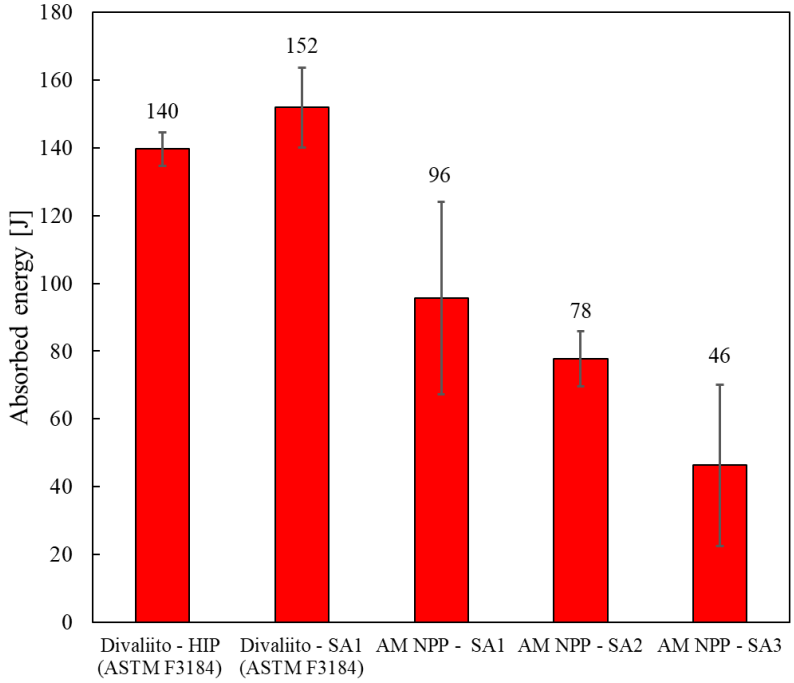

Figure 19. Charpy-V impact energies from DIVALIITO and AM NPP projects

The static tensile properties of the DIVALIITO SA1 and AM NPP SA1 specimens annealed at 1066°C were similar. The HIP specimens in DIVALIITO had nearly identical tensile properties as the high temperature solution annealed AM NPP SA2 and SA3 specimens. The nearly fully recrystallized structure and larger grain size decreased the yield strength of the HIP and SA2 and SA3 specimens compared to specimens heat treated at lower temperatures as expected. Unlike the tensile properties the impact energies differed a lot between the DIVALIITO and AM NPP SA1 specimens as the average impact energy was 56 J lower for AM NPP. In addition, the deviation of the results was much higher for AM NPP compared to DIVALIITO.

4.2 Microstructure

The microstructure of the DIVALIITO specimens was studied with SEM in the same manner as in AM NPP. A side-by-side comparison of SEM images and EBSD maps of both DIVALIITO and AM NPP specimens is shown in Figure 20. The solution annealing of the DIVALIITO SA1 had not removed the anisotropic columnar grain structure formed during the L-PBF process. Many more recrystallized grains can be observed in the AM NPP SA1 specimen compared to the DIVALIITO counterpart. HIP processing and high temperature annealing at 1200°C led to similar grain structure of nearly full recrystallization.

Both the AM NPP and DIVALIITO specimens were decorated with non-metallic inclusions. However the size of the inclusions are notably larger in the AM NPP specimens as shown in Figure 21. Quantitative analysis on the inclusions was not done but significantly larger inclusions were observed in the AM NPP SA1 SEM image. Larger fraction of recrystallized grains indicates the activation energy for recrystallization was lower in the AMM NPP SA1 specimen than for DIVALIITO SA1 after the same thermal post processing. According to (Aota *et al.*, 2021) particle pinning by oxides and other second-phase particles is the main contributor to slower recrystallization in AM alloys compared to conventional material. The size and distribution of these particles affects the boundary movement of nucleated grains via particle pinning (Zener-Smith pinning) and Ostwald ripening. As the particles grow larger at grain boundaries, the pinning force decreases and the boundaries are able to move. They observed coarsening of the inclusions with increasing annealing temperature similarly to our observations. The difference between the recrystallization rate between DIVALIITO and AM

NPP SA1 specimens is due to higher density of preferable nucleation sites for recrystallization in the AM NPP specimens. However, the underlying reason for this phenomenon is left unexplained as more in-depth analysis of the process-structure relationship would be required, which is out of the scope of this study.

In addition, the cellular sub-grain structure which is clearly visible in the DIVALIITO specimen in Figure 21 is absent in the AM NPP specimen. In the DIVALIITO project it was observed the cellular structure remained even after HIP processing. The rapid solidification induced cellular structures, that compose of entangled dislocations, segregation of alloying elements, precipitates and low angle grain boundaries, are considered to have a significant strengthening effect on L-PBF processed materials, including 316L (Voisin *et al.*, 2021). Although the cellular sub-structure was not visible in the AM NPP specimen after annealing at 1066°C, it possibly still exists but might require slightly different surface preparation process to become visible.

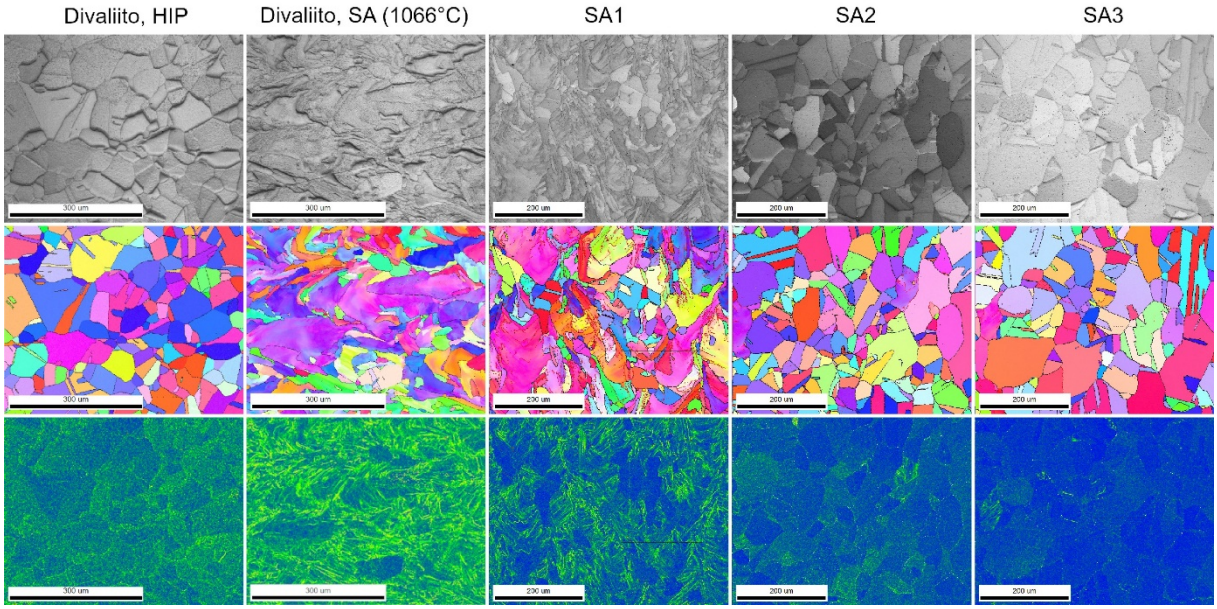

Figure 20. SEM and EBSD images of DIVALIITO and AM NPP specimen cross-sections. In the DIVALIITO images the build direction is towards the right side of the page and in the AM NPP images the build direction is towards the top of the page

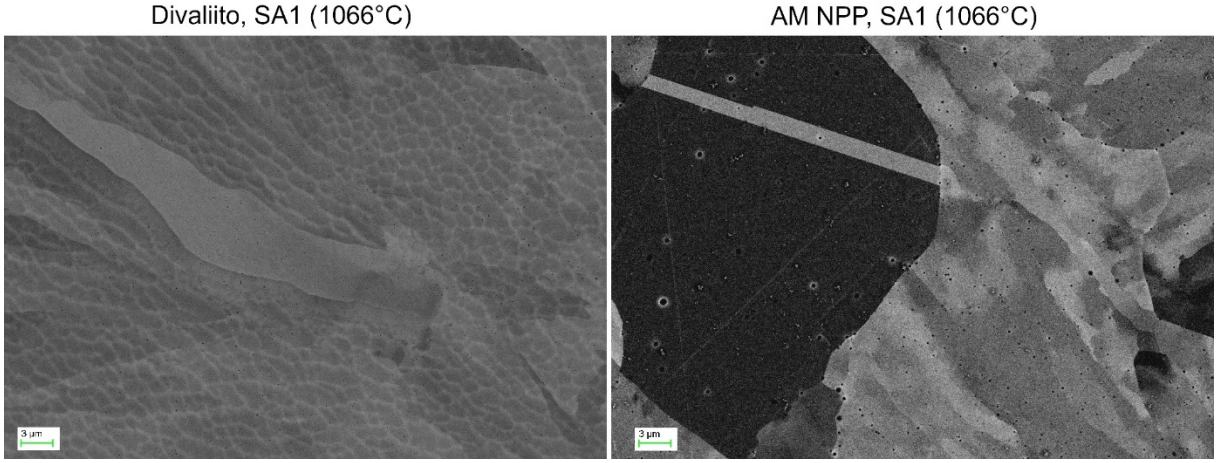

Figure 21. SEM BSE images of DIVALIITO and AM NPP specimens solution annealed at 1066°C

5. Discussion

Our prior studies in DIVALIITO project demonstrated that the standardized solution annealing heat treatment at 1066°C is not sufficient at removing the columnar and highly textured grain structure formed during the L-PBF process. After HIP processing the L-PBF solidification structure was replaced by a recrystallized grains and annealing twins, resembling that of conventional annealed 316L, which is more suitable for nuclear applications. High temperature solution annealing could be a potential substitute for the HIP process as long as the material properties are sufficient.

The microstructure evolves from partially recrystallized anisotropic structure with high density of low angle grain boundaries after annealing at 1066°C to nearly fully recrystallized and stress-free structure at 1200°C as indicated by SEM / EBSD analysis. Inclusions, mainly oxides, were observed in large quantities in all samples and the size of the inclusion increased with higher annealing temperatures. The tensile properties decreased with increasing annealing temperature as expected for a material undergoing recovery, recrystallization and grain growth processes and the SA1 specimens from both projects had comparable tensile properties. All tested specimens fulfilled the minimum requirements for tensile properties in ASTM F-3184. However the microstructure of the AM NPP SA1 specimen differed from the DIVALIITO counterpart as it had higher fraction of recrystallized grains and considerably larger inclusions. Large inclusions are not as effective at reducing grain boundary mobility compared to small inclusions, which in part explains the difference in the grain structures. However based on the analysed data the root cause for different microstructures after identical processing routes can not be explained. Based SEM analysis, a cellular sub-grain structure characteristic to rapid solidification process inherent to the L-PBF process was observed in all DIVALIITO specimens. Similar structure was not seen in the AM NPP SEM images, which could be the result of the sample preparation process.

The most obvious difference between the DIVALIITO and AM NPP specimens was the average impact energy, which were significantly lower for AM NPP specimens. The average impact energy of AM NPP SA1 was 58 J lower compared to DIVALIITO SA1 and the impact energies decreased with increasing solution annealing temperature. As-built L-PBF 316L structure has been shown to have higher impact energies compared to annealed material (Reijonen *et al.*, 2021) and it can suspected the partially recrystallized structure and larger inclusion size degrade the impact properties of the AM NPP SA1 specimen compared to the DIVALIITO counterpart. The average impact energy in SA3 (1200°C) condition was below the minimum impact energy requirement of 40 J defined in SFS-EN 1348. In DIVALIITO the average impact energies in SA1 and HIP conditions were 140J and 152J respectively. Significant quantities of large inclusions were observed in both HIP and the SA2 (1150°C) and SA3 (1200°C) specimens and therefore the inclusions alone do not explain the low impact energies of the AM NPP specimens. Based on the OES chemical analysis no significant oxygen pick up was detected during the L-PBF process and the chemical compositions of printed parts in both projects were comparable. The possibility of feedstock powder oxidation during storage was considered but no excess oxygen was detected, as the oxygen content had remained stable over the 14 months of powder storage between the two projects.

6. Conclusions

The standardized method of solution annealing L-PBF 316L at 1066°C was not sufficient at removing the highly anisotropic structure induced by the manufacturing process. Solution annealing treatments at 1150°C and 1200°C resulted in more homogenous microstructure characterized by recrystallized grains and annealing twins. At 1200°C, the grain structure had almost completely recrystallized according to SEM and EBSD analysis. Abundance of non-metallic inclusions were observed in all conditions where the inclusions grew in size as the annealing temperature increased. In terms of tensile properties, the high annealing temperatures resulted in sufficient strength and ductility, but the impact energies were below the minimum requirement of 40 J. The results from this study were compared to the results of DIVALIITO project in which an identical experimental arrangement was conducted except for the heat treatment cycles. It was found the same process route led to different microstructure and material properties for the standardized heat treatment. In AM NPP specimens the Charpy-V impact energies were considerably lower compared to DIVALIITO. A possible explanation for the difference is the partially recrystallized structure and larger inclusion size in the AM NPP specimen.

Based on our research results, the high temperature solution annealing produced a nearly fully recrystallized and stress-free grain structure similarly to HIP processing. However, the impact energies were low for the solution annealed material, and high deviation of results indicate the microstructures vary between specimens with the same thermal processing history. Based on our findings the 1200°C solution anneal did not results in satisfactory material properties as the impact energies were considered too low. However, annealing 1150°C yielded higher strength and similar grain structure, and is therefore considered more optimal. This study was only a small investigation and a more extensive heat treatment and testing arrangement should be conducted in order to explore the suitable solution annealing parameters in terms of material structure and performance.

References

Aota, L. S. *et al.* (2021) ‘Recrystallization kinetics, mechanisms, and topology in alloys processed by laser powder-bed fusion: AISI 316L stainless steel as example’, *Materialia*. Elsevier B.V., 20(September), p. 101236. doi: 10.1016/j.mtla.2021.101236.

ASTM International (2016) ‘ASTM F3184 (2016) Standard Specification for Additive Manufacturing Stainless Steel Alloy (UNS S31603) with Powder Bed Fusion’, *Annual Book of ASTM Standards*. West Conshohocken, PA 19428-2959, United States, pp. 1–9. Available at: http://www.ansi.org.

Charmi, A. *et al.* (2021) ‘Mechanical anisotropy of additively manufactured stainless steel 316L: An experimental and numerical study’, *Materials Science and Engineering A*. Elsevier B.V., 799(June 2020), p. 140154. doi: 10.1016/j.msea.2020.140154.

Repair Applications Division, J.A. Jones Applied Research Company, EPRI NDE Center (1985) ‘Nuclear Grade Stainless Steel Procurement, Manufacturing and Fabrication Guidelines’. BWR Owners Group and Electric Power Research Institute.

Kong, D. *et al.* (2019) ‘Mechanical properties and corrosion behavior of selective laser melted 316L stainless steel after different heat treatment processes’, *Journal of Materials Science and Technology*. The editorial office of Journal of Materials Science & Technology, 35(7), pp. 1499–1507. doi: 10.1016/j.jmst.2019.03.003.

Lou, X. *et al.* (2017) ‘On the stress corrosion crack growth behaviour in high temperature water of 316L stainless steel made by laser powder bed fusion additive manufacturing’, *Corrosion*

Science, 128. doi: 10.1016/j.corsci.2017.09.017.

Metsä-Kortelainen, S. *et al.* (2020) *New business from digital spare parts (DIVALIITO)*. Available at: https://cris.vtt.fi/en/projects/new-business-from-digital-spare-parts.

Rebak, R. B. and Lou, X. (2018) 'Environmental Cracking and Irradiation Resistant Stainless Steels by Additive Manufacturing', *Bonisteel Blvd*, pp. 1–98. doi: 10.2172/1431212.

Reijonen, J. *et al.* (2021) 'Cross-testing laser powder bed fusion production machines and powders: Variability in mechanical properties of heat-treated 316L stainless steel', *Materials and Design*. The Author(s), 204, p. 109684. doi: 10.1016/j.matdes.2021.109684.

Riabov, D. *et al.* (2021) 'Investigation of the strengthening mechanism in 316L stainless steel produced with laser powder bed fusion', *Materials Science and Engineering A*, 822(June). doi: 10.1016/j.msea.2021.141699.

Voisin, T. *et al.* (2021) 'New insights on cellular structures strengthening mechanisms and thermal stability of an austenitic stainless steel fabricated by laser powder-bed-fusion', *Acta Materialia*. Elsevier Ltd, 203. doi: 10.1016/j.actamat.2020.11.018.